Journal of Zhejiang University-SCIENCE A (Applied Physics & Engineering) 2024 25(9):687-700
www.jzus.zju.edu.cn; www.springer.com/journal/11582
E-mail: jzus_a@zju.edu.cn

Research Article
https://doi.org/10.1631/jzus.A2300449

# Design of a 35 kV high-temperature superconducting synchronous machine with optimized field winding

Chao LUO[1], Bowen XU[1], Jien MA[1]✉, Jiancheng ZHANG[2], Jiabo SHOU[1], Youtong FANG[1]

[1]*College of Electrical Engineering, Zhejiang University, Hangzhou 310027, China*
[2]*Electric Power Research Institute of State Grid Zhejiang Electric Power Corporation, Hang Zhou 310014, China*

**Abstract:** This paper proposes the application of high-voltage stator-cable windings in superconducting machines, based on the characteristics of strong magnetic fields and large air gaps. Cross-linked polyethylene cable winding can be employed to achieve a rated voltage of 35 kV in direct-current (DC)-field superconducting machines, thereby enabling a direct connection between the superconducting machine and the power grid, eliminating the need for transformers. We first, through finite element analysis, demonstrate that the proposed high-voltage high-temperature superconducting machine not only meets the requirement of a 35 kV-rated voltage, but also exhibits minimal flux leakage, torque fluctuation, and harmonic distortion. We then compare three candidate types to discuss the tradeoff between the multi-group superconducting field winding arrangement and machine performances. We propose inverted trapezoidal superconducting field winding as a promising candidate, because it has minimal superconductivity material usage, the largest safety margin for the superconducting coils (SCs), low thrust ripple, and low total harmonic distortion with the desired 35 kV-rated voltage. Finally, through large-scale design parameter sweeping, we show how we selected the optimal parameters for field winding and validated them by the finite element method.

**Key words:** High-voltage stator-cable windings; Superconducting machines; Inverted trapezoidal field winding; Total harmonic distortion

## 1 Introduction

In recent years, superconducting machines have been regarded as promising new equipment for industrial and transportation applications, offering steady reductions in the cost of superconducting materials and continuous improvements in their performance (Masson and Luongo, 2005; Muttaqi et al., 2019; Cucciniello et al., 2022; Sun, 2022). They exhibit remarkable benefits such as compact structure, superior efficiency, and high torque density (Terao et al., 2019; Dias et al., 2022). These characteristics have made them a standard solution for space-sensitive applications such as offshore platforms (Hsieh et al., 2013; Fang et al., 2015; Wang et al., 2015).

Superconducting machines can be divided into two primary categories: fully superconducting machines (Kovalev et al., 2019; Manolopoulos et al., 2020; Liu et al., 2021; Balachandran et al., 2022) and direct-current (DC)-field superconducting machines. The development of fully superconducting machines is currently confined to the realm of theoretical research (Komiya et al., 2020). Superconducting machines are largely commercialized as DC-field types, in which DC-field excited superconducting windings are employed in the rotor and traditional copper windings are adopted for the stator. During the era of low-temperature superconductivity (LTS), these machines demonstrated their reliability, with a 70 MW LTS motor in Japan running stably for 1500 h with a rated voltage of 10 kV (Oishi and Nishijima, 2002). Bong et al. (2019) outlined a design investigation into a 40 MW synchronous motor featuring no-insulation (NI) high-temperature superconducting (HTS) field windings. The rated voltage of 6.6 kV indicated a high rated current. A 10 MW fully superconducting generator with HTS superconducting tapes was studied by Komiya et al. (2019).

---

✉ Jien MA, majien@zju.edu.cn
Chao LUO, https://orcid.org/0000-0003-0756-1508
Jien MA, https://orcid.org/0000-0001-9080-8668

Received Sept. 1, 2023; Revision accepted Dec. 20, 2023;
Crosschecked Aug. 7, 2024

The rated voltage of the motor was 6.9 kV. The China Southern Power Grid Corporation proposed the electromagnetic design for a 10 Mvar DC-field HTS synchronous condenser in 2021 (Duan et al., 2022). The rated voltage of this motor was 11 kV, which meant that it needed to be connected to the grid with a transformer to adjust the reactive power. In the above examples, the power density of the machines was significantly improved by employing high-current-density superconducting field windings. However, almost all DC-field superconducting machines are conventional machines with the addition of superconducting rotors. The full potential advantages of superconducting machines remain underutilized, thus limiting the widespread adoption and implementation of DC-field superconducting machines. Moreover, the majority of DC-field superconducting machines have voltage ratings below 13.8 kV, necessitating their connection to the grid through a transformer.

In order to further improve the power density of superconducting machine systems, the primary objective of this study was to investigate superconducting machines that can be directly connected to the grid to further increase the power density of the system. Superconducting machines offer excellent advantages over traditional room-temperature high-voltage machines (Sumption et al., 2020; Liu et al., 2022), including a remarkably high magnetic field and non-magnetic stator teeth, which cause the voltage to exhibit very low levels of total harmonic distortion (THD). This design also creates additional room to accommodate the high-voltage armature windings, enabling a substantial augmentation in the number of winding turns. Therefore, in this study, cross-linked polyethylene (XLPE) cable winding was employed to achieve a rated voltage of 35 kV in the DC-field superconducting machines, thereby enabling a direct connection between the superconducting machine and the power grid, and eliminating the need for transformers (Lee et al., 2014; Gao et al., 2019; Li et al., 2023). This advancement significantly enhances the short-circuit capacity and power density of the system. This paper presents a comprehensive design and optimization process for high-voltage high-temperature superconducting (HVHTS) machines. The field winding was optimized to meet the low THD of the voltage required by the grid while minimizing the amount of superconducting tape. In addition, it was necessary to combine the properties of superconducting materials and design the structure of the superconducting magnet coil to weaken the influence of sensitive angle fields on critical current and improve the utilization efficiency of the superconducting material. Finally, an inverted trapezoidal field winding HVHTS machine was validated and appeared to be a promising candidate.

The rest of this paper is organized as follows. The structure of the HVHTS motor and the design method and theory are presented in Section 2. In Section 3, the electromagnetic performances of three candidates for the machine design are compared. In Section 4, the influences of several key parameters of the proposed HVHTS machine are discussed in detail. Section 5 concludes the paper.

## 2 Design of high-voltage superconducting machines

The basic design for 35 kV HTS synchronous machines employs a DC HTS field winding. An ultra-high-voltage stator using XLPE cable winding is employed to achieve a rated voltage of 35 kV. The proposed HVHTS machines incorporate a stator back iron made of laminated iron. The rotor employs four double-pancake HTS coils for the rotor field winding, and a slotless stator and a coreless rotor are chosen. Fig. 1 shows the topology of the proposed HVHTS machine.

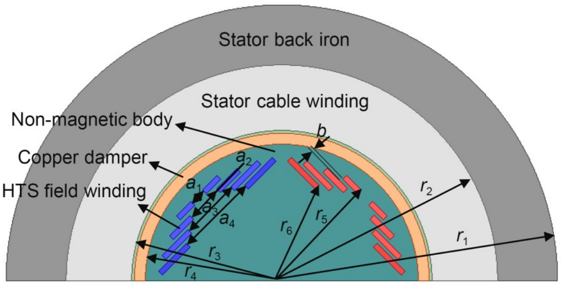

**Fig. 1 Topology of the proposed HVHTS machine. $a_1$–$a_4$ are the inner diameters of the four double-pancake HTS coils; $r_1$ is the stator outer radius; $r_2$ is the stator inter radius; $r_3$ is the armature coil inter radius; $r_4$ is the damper inter radius; $r_5$ is the field coil outer radius; $r_6$ is the field coil inter radius; $b$ is the vertical pitch between the trapezoidal superconducting field coils of the rotor**

In the design of superconducting machines, critical factors such as terminal voltage and rotor speed are principally dictated by the power system. These parameters establish the design criteria for the machines. In this section, we explain the design of a DC-field HTS machine with a rated line voltage of 35 kV.

### 2.1 Stator design

Currently, almost all synchronous machines are designed with a limitation on their output voltage, capping it at 25 kV. Asea Brown Boveri (ABB) has successfully conducted experiments with cable insulation for high-voltage generators rated at 45 kV, and successfully connected them to the grid at the Purjus hydroelectric power station in Sweden (Perers et al., 2007). It is noteworthy that high-voltage cables equipped with XLPE insulation have now been improved further, reaching voltages of up to 500 kV (Metwally et al., 2008).

The key to designing the stator with a rated voltage of 35 kV is to determine the cable diameter. According to Hao et al. (2012), the electric field in the stator winding is distributed between the inner and outer semiconductor layers of the cable. The cable capacitance per unit length $C_0$ between the inner and outer semiconductor layers can be calculated from

$$C_0 = \frac{1.778\times 10^{-11}\pi m_1}{\ln\left(\frac{r_{a1}}{r_{a2}}\right)}, \tag{1}$$

where $m_1$ is the relative permittivity ($m_1$=2–3), $r_{a1}$ is the outer radius of the inner semiconductor layer, and $r_{a2}$ is the inner radius of the outer semiconductor layer.

However, $C_0$ varies at different positions along the winding as the insulation thickness of the cable increases gradually from the neutral to the terminal (Tian and Lin, 2006). As an example, we will use a two-segment cable as a model for high-voltage winding, as shown in Fig. 2. The proportion between the two segments is $a/(1-a)$. $U_1$ and $U_2$ are terms used to denote neutral voltage and terminal voltage, respectively. The capacitances per unit length for the first and second segments are represented by $C_1$ and $C_2$, respectively. The entire length of the winding is denoted as $l$. The voltage per unit length of phase 1 in the winding, represented by $E_{12}$, has a relationship with the neutral and terminal voltages:

$$\dot{E}_{12}l = \dot{U}_1 - \dot{U}_2. \tag{2}$$

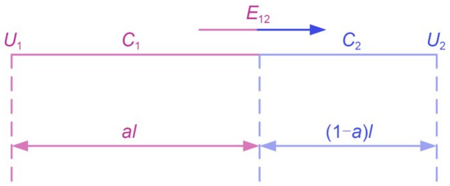

**Fig. 2 Two-segment cable**

The capacitive current $I_1$ of phase 1 during normal operation can be calculated as follows:

$$\dot{I}_1 = \mathrm{j}\omega\int_0^{al}\dot{E}_{12}xC_1\mathrm{d}x + \mathrm{j}\omega\int_{al}^{1}\dot{E}_{12}xC_2\mathrm{d}x, \tag{3}$$

where j is the imaginary unit, and $\omega$ is the angular frequency.

Consider a high-voltage synchronous machine operating at 35 kV. The stator-cable winding of the HVHTS machine, as depicted in Fig. 3, is configured with 10 cables within each slot. After the rated voltage and rated current of the motor are determined, the insulation thickness is determined iteratively according to Eqs. (1)–(3). This paper has simplified that the first five cables nearest to the rotor surface are rated for 10 kV, while the remaining five cables are 20 kV. The fundamental design parameters for this 35 kV stator-cable winding are provided in Table 1.

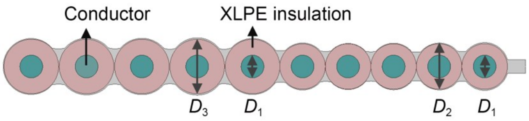

**Fig. 3 Slot of a 35 kV high-voltage stator with 10 cables**

**Table 1 Cable configuration of high-voltage stator**

| Parameter | Value |
|---|---|
| Diameter of conductor, $D_1$ (mm) | 10 |
| Diameter of 10 kV cable, $D_2$ (mm) | 20 |
| Diameter of 20 kV cable, $D_3$ (mm) | 24 |
| Slot width of 10 kV cable (mm) | 22 |
| Slot width of 20 kV cable (mm) | 26 |

### 2.2 HTS field-winding design

In this study, for a more sinusoidal air-gap magnetic-field waveform, the rotor had four pairs of double-pancake superconducting coils (SCs) arranged in a stepped/tiered fashion. Taking into consideration the support and fixation, the cross-sectional structure of the SCs could not be allowed to exceed the rotor's virtual contour line (shown in Fig. 4). By choosing a suitable air gap between the inner radius of the stator armature winding ($r_3$) and the radius of the rotor field winding

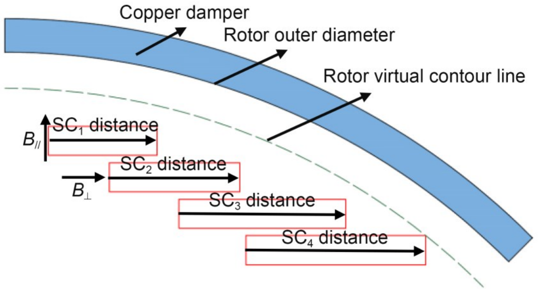

**Fig. 4 Constraints on the superconducting field coils. $B_\perp$ and $B_{//}$ are the magnitudes of the magnetic field perpendicular and parallel to the superconducting strip, respectively**

($r_6$), the total magnetomotive force (MMF) of the rotor HTS windings could be represented (Miller and Hughes, 1977; Abrahamsen et al., 2009; Seo et al., 2023). This representation is a function of the magnetic flux density $B_s$, the average radius $r_b$, the turn number of field winding $N_{bf}$, the field current $i_{bf}$, the pole number $p$, the air permeability $\mu_0$, and the rotor field winding radius $r_f$:

$$N_{bf}i_{bf}=\frac{\pi r_f B_s}{\mu_0\left(\frac{r_f}{r_b}\right)^{p+1}\left[1+\left(\frac{r_b}{r_2}\right)^{2p}\right]}. \tag{4}$$

The $B_s$ in Eq. (4) is calculated as follows:

$$B_s=\frac{\mu_0 N_{bf}i_{bf}r_f}{D^2}\left[1+\left(\frac{r_b}{r_2}\right)^2\right], \tag{5}$$

where $D$ is the armature mean winding diameter.

Setting the cross-sectional area of each SC to $A_{wire}$ and the total cross-sectional area of the excitation coil to $A_{coil}$, turns of field winding $N_{bf}$ is:

$$N_{bf}=\frac{A_{coil}}{A_{wire}}. \tag{6}$$

### 2.3 Kim-like model for superconducting properties

The SC can only maintain superconducting properties when the incoming current is less than the critical current. Kim et al. (1964) pointed out that the critical current density of a superconductor is not only dependent on temperature, but also on the external magnetic field. In this analysis, it is assumed that the critical current decreases most significantly due to magnetic fields perpendicular to the tape face, which allows the application of a Kim-like model (Kim et al., 1964), as:

$$I_c(B_\perp, B_{//})=\frac{I_{c0}}{\left(1+\frac{\sqrt{kB_{//}^2+B_\perp^2}}{B_c}\right)^\alpha}, \tag{7}$$

where $I_c$ is the critical current, $I_{c0}$ is the critical current under the self-field of the superconducting strip, $B_\perp$ and $B_{//}$ are the magnitudes of the magnetic field perpendicular and parallel to the superconducting strip, respectively, and $k$, $\alpha$, and $B_c$ are the parameters fitted by experimental data. Fig. 5 illustrates the variation of the critical current of rare earth barium copper oxide (REBCO) with respect to the parallel and perpendicular external magnetic fields at 30 K. This constraint primarily influences the selection of the field current.

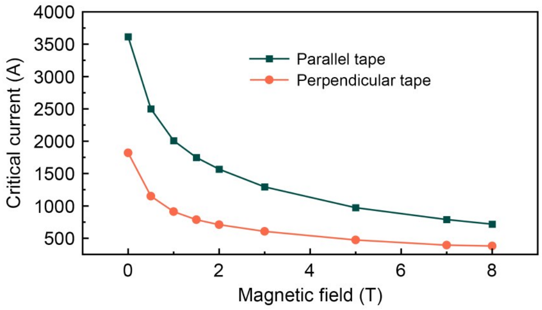

**Fig. 5 Variation in critical current of HTS with magnetic field**

## 3 Electromagnetic performance analysis

For comprehensive design and optimization of HVHTS machines, it is vital to develop a precise model. Consequently, we employed the finite element method (FEM), as shown in Fig. 6. Simulations were carried out using the full model, utilizing the Maxwell transient

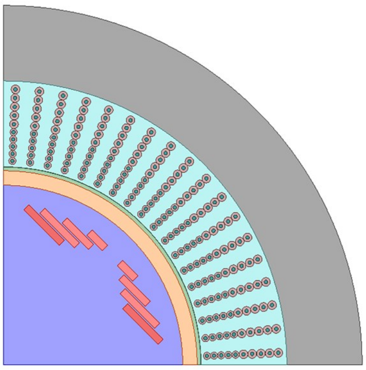

**Fig. 6 1/4 2D FEM model of a 15 MW HVHTS machine**

solver with a 0-vector-potential boundary for the outer arc of the stator back iron. To delve deeper into the influence of the stator-rotor end, we generated a 3D finite element model (Fig. 7). However, owing to the substantial computational load, the 3D finite element calculation required 14 h per iteration. This extended time frame was a result of predominantly utilizing a 2D finite element approach for the optimized design. In this section, we describe the quantitative comparison of three typical types (I–III) of HVHTS machines by FEM. As can be seen in Fig. 10, the three counterparts have the same stator structure. The detailed geometric parameters are listed in Table 2. Type II and type III rotors employ four pairs of double-pancake SCs with a trapezoidal layout, characterized by a stepwise increase of SCs from the topmost to the lower SCs. In contrast, type I employs an inverted trapezoidal layout, characterized by a stepwise decrease of SCs from top to bottom. Notably, type II situates the topmost coil closer to the air gap, while types I and III share a similar positioning. The number of SCs in type III is 2026, which is 110% and 102% of the numbers in types I and II, respectively.

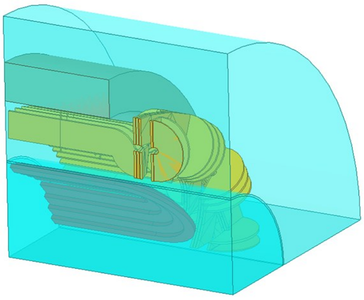

**Fig. 7 1/16 3D FEM model of a 15 MW HVHTS machine**

Fig. 8 shows the open-circuit phase back-EMF (electromotive force) waveforms of the three candidates, and Fig. 9 shows the corresponding spectra. One of the main objectives of this study was to improve the voltage waveforms, which is outlined and extensively discussed in this section. It is notable that the amplitude of type II is 3.7% higher than that of type I. Fig. 9 also shows the existence of high synchronization between the back-EMF and the corresponding spectra in types I and III. In all three candidates, the low values of the third and fifth harmonic amplitudes demonstrated the proper design of the proposed machine. In addition, the THD of the voltage waveform was calculated to be less than 5.1%, 9.3%, and 5.3% for types I, II, and III, respectively. The results reveal that the peak value of the phase voltage amounts to approximately 27.8 kV, while the effective value of the phase voltage reaches around 19.7 kV. Consequently, the rated three-phase voltage adequately fulfills the stipulated 35 kV requirements.

**Table 2 Design parameters of types I–III**

| Parameter | Value | | |
|---|---|---|---|
| | Type I | Type II | Type III |
| Rated voltage (kV) | 35 | 35 | 35 |
| Speed (r/min) | 1500 | 1500 | 1500 |
| Pole number | 4 | 4 | 4 |
| Slot number | 72 | 72 | 72 |
| Stator outer radius, $r_1$ (mm) | 1010 | 1010 | 1010 |
| Stator inter radius, $r_2$ (mm) | 790 | 790 | 790 |
| Effective length (mm) | 1175 | 1175 | 1175 |
| Operating current (A) | 480 | 480 | 480 |
| Damper inter radius, $r_4$ (mm) | 500 | 500 | 500 |
| Damper outer radius (mm) | 540 | 540 | 540 |
| Armature coil inter radius, $r_3$ (mm) | 551 | 551 | 551 |
| Armature coil outer radius, $r_2$ (mm) | 790 | 790 | 790 |
| SC width (mm) | 10 | 10 | 10 |
| SC thickness (mm) | 0.4 | 0.4 | 0.4 |
| Field coil outer radius, $r_5$ (mm) | 441 | 461 | 441 |
| Field coil inter radius, $r_6$ (mm) | 376 | 394 | 376 |
| Number of coils $SC_1$ | 610 | 340 | 376 |
| Number of coils $SC_2$ | 530 | 490 | 450 |
| Number of coils $SC_3$ | 424 | 560 | 574 |
| Number of coils $SC_4$ | 276 | 600 | 626 |
| Total coil number | 1840 | 1990 | 2026 |
| $b$ (mm) | 5 | 5 | 5 |
| $a_1$ pitch (mm) | 60 | 60 | 60 |
| $a_2$ pitch (mm) | 218 | 140 | 144 |
| $a_3$ pitch (mm) | 360 | 240 | 240 |
| $a_4$ pitch (mm) | 490 | 300 | 352 |

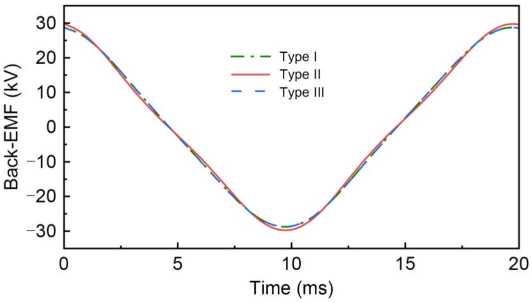

**Fig. 8 Comparison of phase back-EMF waveforms**

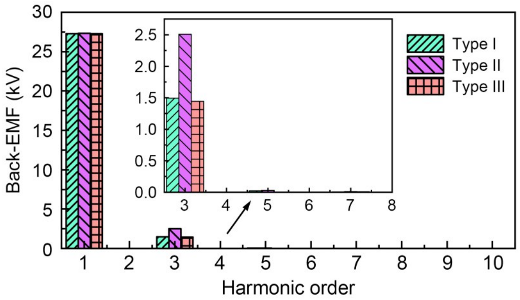

**Fig. 9 Comparison of phase back-EMF spectra**

It is evident from Fig. 10 that the average torques for all three types are almost identical, with each type globally optimized to achieve the maximum average torque while adhering to the constraint of 4.3 kW copper loss, approximately 91.20 kNm, owing to the equal fundamental component of the magnetic field within the air gap. Upon achieving a steady state, the torque for type II peaks at 91.38 kNm, in contrast to the minimum value of 91.00 kNm, resulting in a torque fluctuation of approximately 0.38 kNm. Furthermore, many peaks are apparent in the type II curve. Compared with the torque ripple in type II, 28.6% and 63.0% torque-ripple reduction is achieved for types I and III, respectively. The results of our calculations demonstrate that when the sides of the stator are identical, type I employs 7.5% and 9.2% fewer SCs compared to types II and III, respectively. Moreover, despite this reduction, type I can generate the same average torque with a significantly lower torque ripple.

As depicted in Fig. 11, the 3D finite element analysis outcomes reveal that comparable results can be achieved. This is because the superconducting rotor end generates a robust magnetic field, causing the magnetic lines of force to interlink with the stator. Consequently, all three types of torque appear to increase when the end is taken into account. With an equivalent superconducting usage as in the 2D case, type I maintains the highest average torque and the least torque fluctuation.

Fig. 12 demonstrates the flux-density and flux-line distributions in the cross-section of the three types of

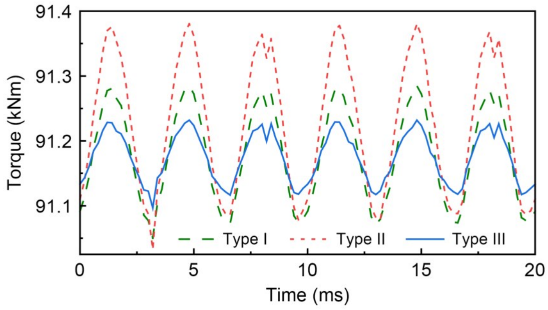

**Fig. 10 Comparison of torque (2D)**

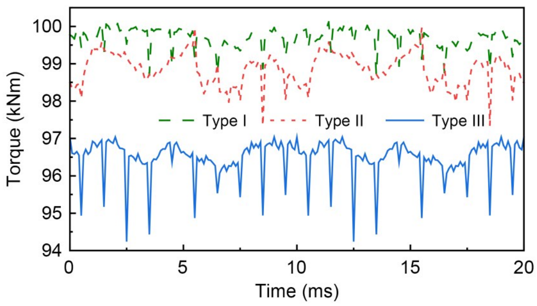

**Fig. 11 Comparison of torque (3D)**

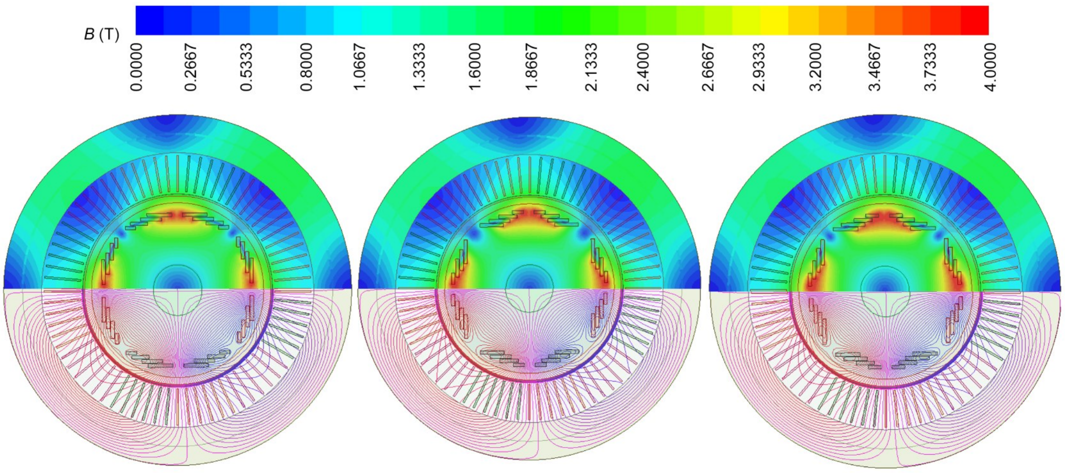

(a) (b) (c)

**Fig. 12 Flux-contour distributions of the three SC candidates: (a) type I; (b) type II; (c) type III**

HVHTS machines. It is clear that the magnitudes of the flux density around the HTS coils are much higher than those around other parts. Moreover, the innermost regions of the SCs in all three types experience by far the highest magnetic field. This indicates that the critical current of an SC is determined by the magnetic field in its innermost regions. Among the three types, the SCs of type I were subjected to the least external magnetic field at their corresponding locations. We attribute this to the fact that all three types of SC operate at the same current density, while type I has the fewest number of coils. Fig. 10 also reveals that the three types have the same main flux through the center of the N-pole coil, the stator yoke, the center of the S-pole coil, and the rotor yoke, with minimal flux leakage. For all three types, flux leakage near the air gap is minor, but the level of flux leakage between the north and south poles of the rotor and the coil is relatively high. This is attributable to the robust magnetic field created by the SCs and the considerable magnetic potential on the stator side. This means that flux leakage does not rise significantly with the widening of the physical air gap in these HVHTS machines.

Because of the symmetry of the rotor coil, we selected only one pole for analysis (Fig. 13), with the upper half divided into the left part of one pole in Fig. 10 and the lower half into the right part. The maximum flux density in all three types is exhibited in the topmost SC. However, the highest flux density in type I is predominantly parallel to the SC, whereas the flux-density components in types II and III are considerably greater in the vertical SC. Apart from the innermost flux lines, which are nearly parallel, all others display curvilinear trajectories, creating a distinct "nucleus point" within the lower coil. Maximum flux leakage is observed in the lower coil, with the flux density at the "nucleus point" being the least.

Based on the information in the first section, the critical current of an SC at the same temperature is determined by the magnitude of the magnetic fields parallel and perpendicular to it. Therefore, we calculated the parallel and perpendicular magnetic fields near the SC in three different scenarios.

The magnetic field in the parallel SC corresponds to the results in Figs. 14–17. When calculating the magnetic field in parallel $SC_1$ and $SC_2$, the absolute of the magnetic field is consistently smaller for type I compared to both types II and III, despite type I having a larger number of coils. Considering $SC_3$, the peak value of type I in the external magnetic field was determined to be 1.8 T. Fig. 16 represents a reduction of approximately 38.7% and 41.9% compared to types II and III, respectively. Similarly, for $SC_4$, the peak value of type I was calculated to be 0.9 T, which corresponds to 34.6% and 40.9% of the values for types II and III, respectively.

Comparing Figs. 14–17, it is apparent that the maximum of the magnetic field in the parallel SC for all three types is located on the innermost side of $SC_1$. The maximum of type III is 4.0 T, which is 104% and 102% of the value for types I and II, respectively. It is worth noting that all three types exist in regions where the magnetic field of the parallel SC is zero.

The distribution of the magnetic field perpendicular to the SC corresponds to the results in Figs. 18–21. We found that the highest perpendicular magnetic field consistently resides in the innermost region of the coil. Notably, if the $SC_1$ distance surpasses 60 mm, the

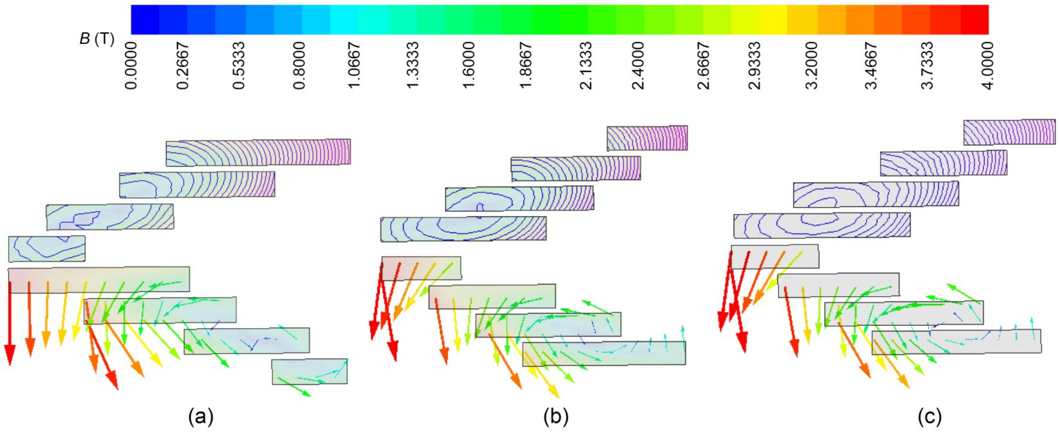

**Fig. 13 Flux-contour distributions of the three SC candidates: (a) type I; (b) type II; (c) type III**

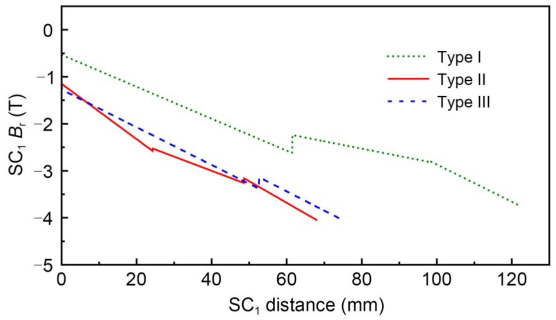

Fig. 14 Comparison of radial magnetic field ($B_r$) of the parallel SC$_1$

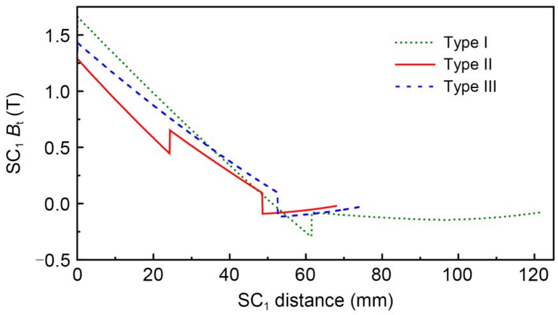

Fig. 18 Comparison of tangential magnetic field ($B_t$) of perpendicular SC$_1$

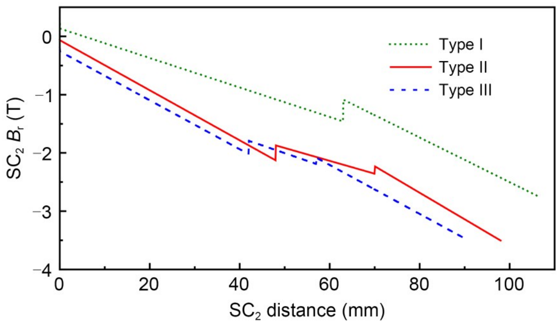

Fig. 15 Comparison of radial magnetic field of the parallel SC$_2$

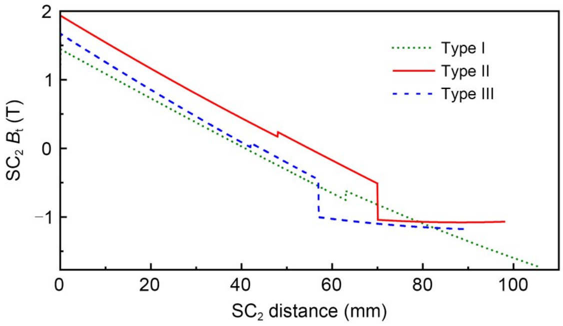

Fig. 19 Comparison of tangential magnetic field of perpendicular SC$_2$

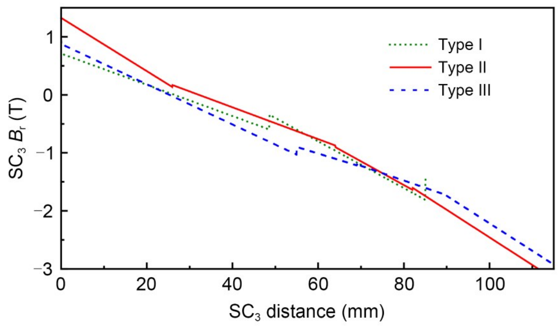

Fig. 16 Comparison of radial magnetic field of the parallel SC$_3$

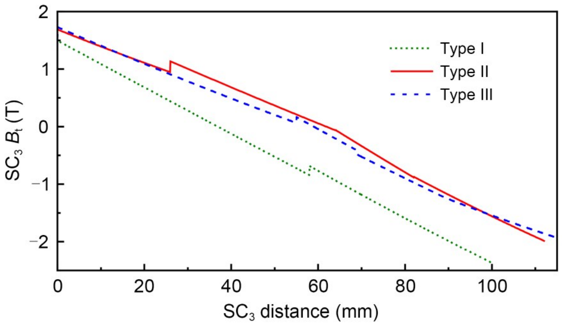

Fig. 20 Comparison of tangential magnetic field of perpendicular SC$_3$

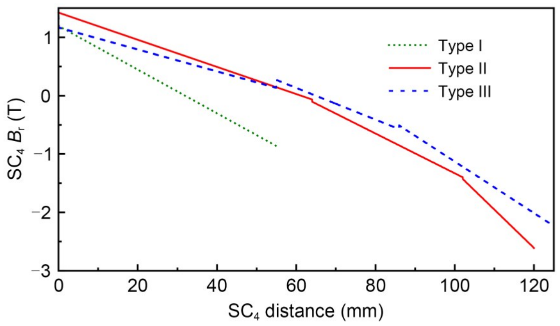

Fig. 17 Comparison of radial magnetic field of the parallel SC$_4$

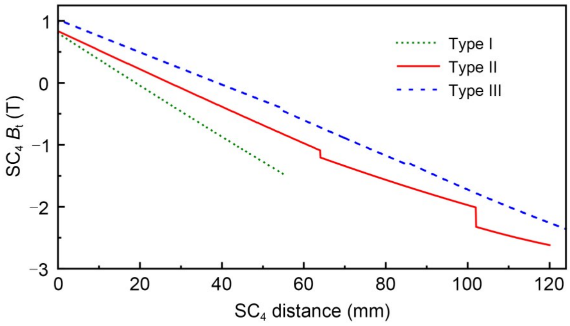

Fig. 21 Comparison of tangential magnetic field of perpendicular SC$_4$

perpendicular magnetic field of the coils maintains a consistent value of approximately −0.1 T, regardless of the increasing distance from $SC_1$. Both types II and III exhibited a peak value of the perpendicular magnetic field of approximately 2.6 T, located within the $SC_3$. Conversely, for type I, the maximum value was slightly lower, approximately 2.4 T, also situated within the $SC_3$. All three types exist in regions where the magnetic field of the perpendicular SC is zero.

It is known that the magnetic field of the perpendicular SC has a more dramatic impact on current density than the magnetic field parallel to it. However, since the magnetic field in a machine is continuously changing in terms of the impact of the magnetic field on HTS coils, it should be treated as a perpendicular field to ensure the safety of HTS coils. Because of this, the SC of type III experienced the highest external magnetic field of all three types, reaching a maximum of 4.1 T. Nevertheless, the SC of type I had the lowest external magnetic field at 3.8 T, with all three types having a field current of 480 A. Furthermore, the field distributions within the coils are much more uniform (smaller field angles) in type I. The variation in the critical current of an HTS with the magnetic field (Fig. 5) confirms that at a temperature of 30 K, the critical current maintains a substantial margin, ensuring the safety of HTS conductors. Consequently, it can be concluded that type I demonstrates the most substantial safety margin for the SC.

In a rotating machine, the interaction between the rotor and the stator is primarily decided by the radial component of the magnetic field generated by the rotor. Consequently, the distribution of the radial magnetic induction intensity produced by the SC is crucial.

As shown in Fig. 22, the $R$=550 mm air-gap radial magnetic fields at the same position in types I and III agree well with one another ($R$ is the distance from the center of the circle to the calculated point). The peak of type III was calculated to be 1.8 T, which is approximately 11.0% and 9.6% higher than those of types I and II, respectively. The corresponding spectra results are shown in Fig. 23. In accordance with the aforementioned design specifications, all three types consistently maintain a primary magnetic field of 1.4 T. It is notable that only the third harmonic components exhibit substantial amplitudes, calculated as 0.23, 0.39, and 0.22 T for the three types.

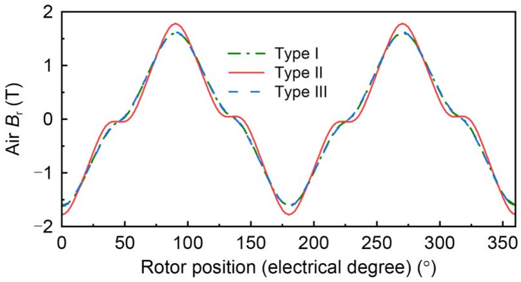

**Fig. 22  Comparison of air-gap radial magnetic field**

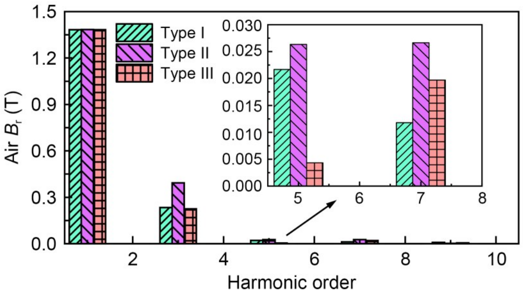

**Fig. 23  Comparison of air magnetic-field spectra**

The $R$=550 mm tangential component of the magnetic field generated by the rotor is the main cause of vibration noise in a rotating machine. Therefore, attention is also paid to the distribution of tangential magnetic induction intensity generated by the SC. As illustrated in Fig. 24, many peaks are apparent in the type II curve. The peak of type II was calculated to be 0.95 T, which is approximately 15.1% and 15.8% higher than types I and III, respectively. As shown in Fig. 25, the spatial distributions of the three types are non-sinusoidal. Types I and III produced almost the same results, with the highest content in type II being 0.38 T.

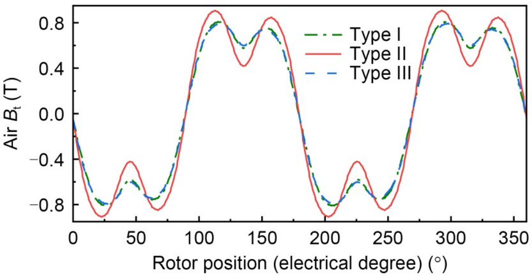

**Fig. 24  Comparison of air-gap tangential magnetic field**

The self and mutual inductances of the three types of HVHTS machines, as determined by 2D finite element analysis, are presented in Figs. 26 and 27. Fig. 26 demonstrates that the mutual inductance amplitudes of the three types of field windings and stator windings

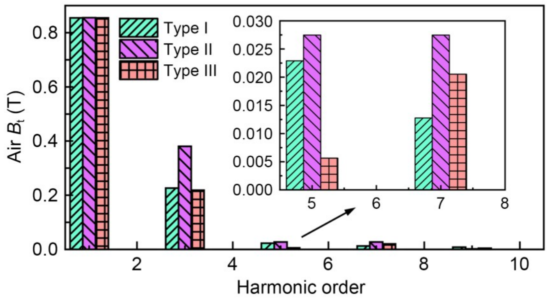

**Fig. 25 Comparison of air-gap tangential magnetic-field spectra**

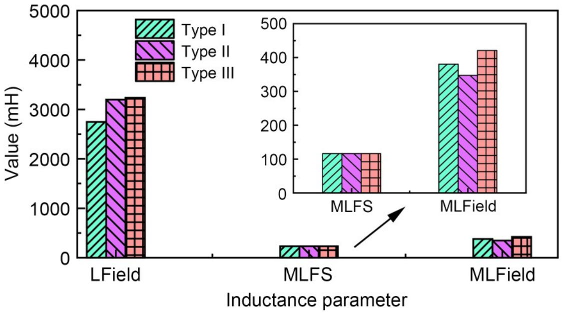

**Fig. 26 Comparison of field-coil self and mutual inductance (2D)**

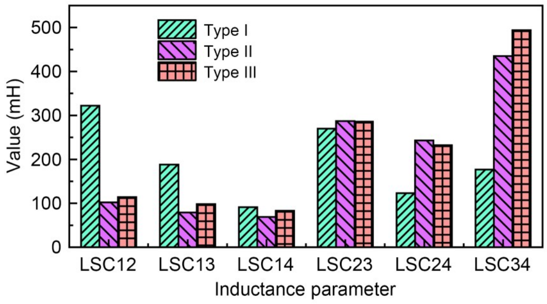

**Fig. 27 Comparison of field-coil mutual inductance (2D)**

(MLFSs) are equal, meeting the previously outlined design requirements for HVHTS machines. Each pole field-winding self-inductance (LField) for type III was calculated to be 3.237 H, which is approximately 17.8% and 1.3% higher than for types I and II, respectively. The mutual inductance of the superconducting field windings of neighboring poles (MLField) for type III was calculated to be 421 mH, which is approximately 10.7% and 21.3% higher than for types I and II, respectively. As can be seen from Fig. 27, the maximum mutual inductance within the SC of type I is 322 mH between $SC_1$ and $SC_2$ (LSC12). In contrast, the maximum mutual inductances within the type II and type III coils are 435 and 494 mH, respectively, both occurring between $SC_3$ and $SC_4$ (LSC34). Increasing the inductance is detrimental to the ability of a machine to rapidly respond to frequent changes in load by adjusting the field current, thereby weakening its transient regulation capability.

Based on 3D finite element analysis, the correlation between the three 3D finite element types closely aligns with the 2D results, predominantly due to a significant enhancement in the 3D outcomes when factoring in the stator-rotor ends. The results reveal that the mutual inductance among the SCs is minimal, indicating a low level of magnetic coupling between them. This means that there is negligible leakage inductance in the field coil (Figs. 28 and 29).

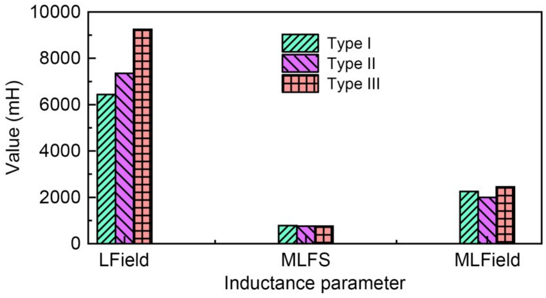

**Fig. 28 Comparison of field-coil self and mutual inductance (3D)**

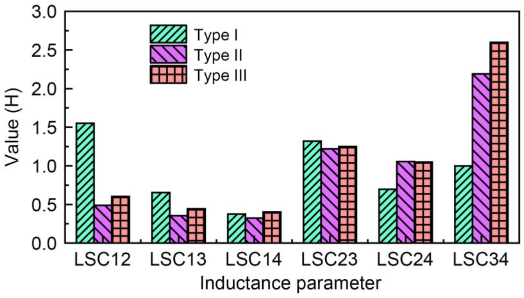

**Fig. 29 Comparison of field-coil mutual inductance (3D)**

## 4 Parameter optimization

The findings described in the sections above made it clear that type I should be considered a promising topology. In this section, we discuss the influence of variations in structural parameters on electromagnetic performance, utilizing the FEM. In order to ensure fairness in the optimization process, we took into account the constraints of equal machine volume, stator heat-dissipation power, and the number of SCs.

### 4.1 Stator back iron

The HVHTS machines incorporate a stator back iron made of laminated iron. The laminated iron shield has the added benefits of reduced energy loss and the potential to serve as a portion of the stator-winding support structure.

Fig. 30 shows the variation in torque and torque ripple with stator environmental shielding thickness. We found that the torque increases and torque ripple decreases immediately when the stator environmental shielding thickness is less than 200 mm. This is because thicker environmental shielding results in a more effective magnetic circuit. Upon achieving a steady state, neither average torque nor torque ripple shows a noticeable change when the stator environmental shielding thickness is increased to up to 220 mm. We therefore selected an environmental shielding thickness of 220 mm.

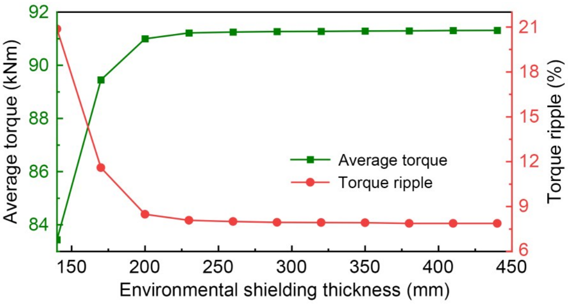

**Fig. 30 Comparison of average torque and torque ripple with different environmental shielding thicknesses**

### 4.2 Damper shield

The damper shield is a distinctive structure of superconducting machines, which protects the superconducting windings from the impact of higher harmonic originating from the stator side. As illustrated in Fig. 31, many peaks are apparent in the curves of a damper shield with a thickness of 13 mm. Moreover, the torque for a damper-shield thickness of 13 mm peaks at 91.46 kNm, in contrast to the minimum value (calculated at 90.90 kNm), resulting in a torque fluctuation of approximately 0.56 kNm. The power output does not show obvious variation, and the torque ripple is significantly reduced with the increase in shield thickness. We therefore determined that the optimal value of damper-shield thickness was 40 mm. The shield-eddy current losses for the three cases are 30.4, 51.0, and 218.2 W. It should be noted that the shield here includes Dewar shield, and a sufficiently thick shield is necessary for effective protection of the SCs under motor transients.

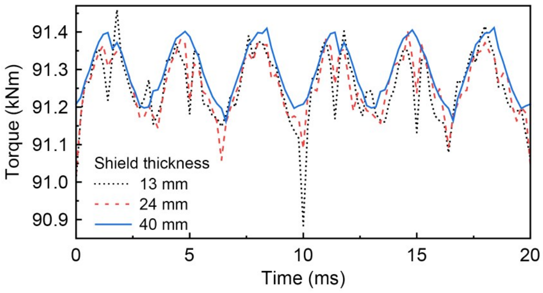

**Fig. 31 Comparison of average torque vs. shield thickness**

### 4.3 HTS coil

The field winding was thus optimized to meet the low total harmonic distortion of the voltage required by the grid. For a more sinusoidal air-gap magnetic-field waveform, the rotor employs four pairs of double-pancake SCs arranged in a stepped/tiered formation. Ensuring air-gap magnetic-field performance and minimizing the costs of superconducting materials are critical factors for the optimization of HVHTS machines. In addition, it is necessary to consider the properties of superconducting materials and design the structure of the SC to weaken the influence of sensitive angle fields on critical current and improve the utilization of the superconducting material.

As illustrated in Fig. 1, *b* denotes the vertical pitch between the trapezoidal superconducting field coils of the rotor. It is presumed that the vertical spacing remains consistent for each coil. As can be seen in Fig. 32, the average torque and torque ripple exhibit an almost linear response to *b*, owing to the proximity of the SC to the stator. However, the SC must be securely

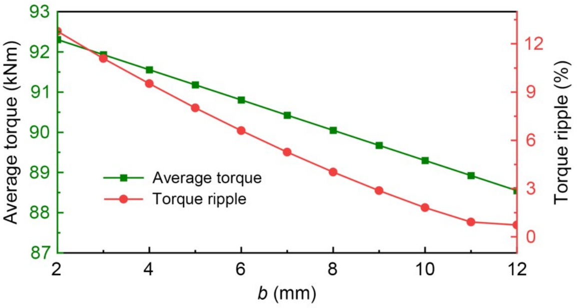

**Fig. 32 Comparison of average torque and torque ripple vs. *b***

positioned between the structures, necessitating a suitable distance between them. Therefore, it is essential to ensure that the spacing between the coils, denoted as *b*, is not overly compact. The optimal value of *b* was determined to be 5 mm.

The $a_1$–$a_4$ are defined as the inner diameters of the four double-pancake HTS coils. Figs. 33–36 show that the average torque increases positively with the pitch for $a_1$, $a_2$, $a_3$, and $a_4$. Ideally, maximizing the value of $a_1$ among the four horizontal distance variables would yield the highest torque-lifting efficiency, due to the linear decrease in the distance from the stator. However, the torque ripple will be considerably boosted as the $a_1$ pitch increases. With a value of 120 mm for $a_1$, the torque ripple reaches a substantial value of 22%. The torque ripple decreases with $a_2$ pitch first, then reaches a minimum value, and increases linearly from 2% to 9%. As the $a_3$ pitch increases from 160 to 380 mm, the torque ripple first drops and then increases linearly from 2% to 9%. It is evident that when the $a_4$ pitch increases, the torque ripple increases slightly, and then decreases sharply at the $a_4$ pitch of 500 mm.

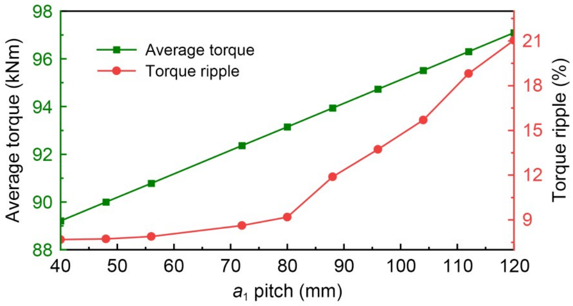

**Fig. 33 Comparison of average torque and torque ripple vs. $a_1$ pitch**

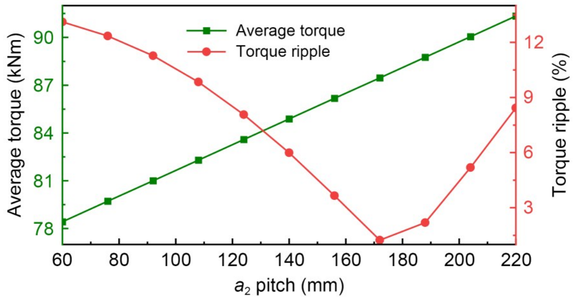

**Fig. 34 Comparison of average torque and torque ripple vs. $a_2$ pitch**

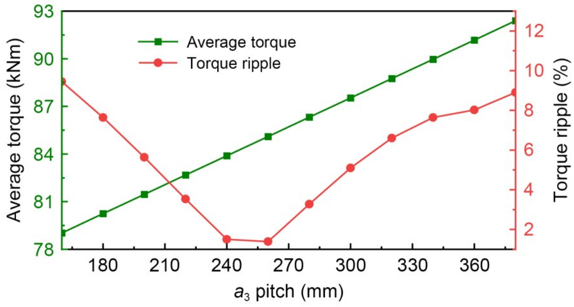

**Fig. 35 Comparison of average torque and torque ripple vs. $a_3$ pitch**

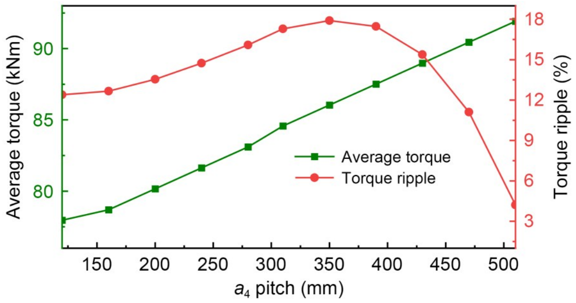

**Fig. 36 Comparison of average torque and torque ripple vs. $a_4$ pitch**

## 5 Conclusions

We propose a rated voltage of 35 kV in a DC-field superconducting HVHTS machine. In our model, the machine is considered to be applied in a 35 kV power grid, eliminating the utilization of transformers. Three candidate types are compared to discuss the tradeoff between the multi-group superconducting field-winding arrangement and machine performances. In addition, we propose an inverted trapezoidal field winding, which experiences the smallest external magnetic field at merely 3.8 T. The number of SCs in the candidate type I is 1840, which is 92.4% and 90.8% of the numbers for the other two types. Furthermore, the THD of the voltage waveform is calculated to be less than 5.1%. The orientation of the strongest magnetic fields in the most promising candidate is predominantly parallel to the SC, which also indicates the most substantial safety margin for the SC. The magnetic-field peak for type II is calculated to be 0.95 T, approximately 15.1% and 15.8% higher than the peaks for types I and III, respectively. Thus, the results reveal that the mutual inductance among the SCs is minimal, signifying a low level of magnetic coupling between them; this indicates negligible leakage inductance in the field coil.

## Acknowledgments

This work is supported by the State Grid Corporation of China R&D Project (No. 5500-202319193A-1-1-ZN).

## Author contributions

Jien MA designed the research. Chao LUO processed the corresponding data and wrote the first draft of the manuscript. Bowen XU, Jiancheng ZHANG, and Jiabo SHOU helped to organize the manuscript. Youtong FANG revised and edited the final version.

## Conflict of interest

Chao LUO, Bowen XU, Jien MA, Jiancheng ZHANG, Jiabo SHOU, and Youtong FANG declare that they have no conflict of interest.

## References

Abrahamsen AB, Mijatovic N, Seiler E, et al., 2009. Design study of 10 kW superconducting generator for wind turbine applications. *IEEE Transactions on Applied Superconductivity*, 19(3):1678-1682. https://doi.org/10.1109/TASC.2009.2017697

Balachandran T, Yoon A, Lee D, et al., 2022. Ultrahigh-field, high-efficiency superconducting machines for offshore wind turbines. *IEEE Transactions on Magnetics*, 58(2): 8700805. https://doi.org/10.1109/TMAG.2021.3094163

Bong U, An S, Voccio J, et al., 2019. A design study on 40 MW synchronous motor with no-insulation HTS field winding. *IEEE Transactions on Applied Superconductivity*, 29(5): 5203706. https://doi.org/10.1109/TASC.2019.2908548

Cucciniello N, Lee D, Feng HY, et al., 2022. Superconducting niobium nitride: a perspective from processing, microstructure, and superconducting property for single photon detectors. *Journal of Physics: Condensed Matter*, 34(37):374003. https://doi.org/10.1088/1361-648X/ac7dd6

Dias FJM, Sotelo GG, de Andrade Júnior R, 2022. Performance comparison of superconducting machines with induction motors. *IEEE Transactions on Applied Superconductivity*, 32(7):5202805. https://doi.org/10.1109/TASC.2022.3188461

Duan XH, Shi ZJ, Song M, et al., 2022. Application prospects of the superconducting dynamic synchronous condenser. *IEEE Transactions on Applied Superconductivity*, 32(6): 5202405. https://doi.org/10.1109/TASC.2022.3168497

Fang K, Qiu LM, Jiang X, et al., 2015. Temperature inhomogeneity in high capacity pulse tube cryocoolers. *Journal of Zhejiang University-SCIENCE A (Applied Physics & Engineering)*, 16(11):910-921. https://doi.org/10.1631/jzus.A1400296

Gao CF, He DX, Zhou YF, et al., 2019. A study on the space charge characteristics of AC sliced XLPE cables. *IEEE Access*, 7:20531-20537. https://doi.org/10.1109/ACCESS.2019.2893604

Hao LL, Sun YG, Qiu AR, et al., 2012. Steady-state calculation and online monitoring of interturn short circuit of field windings in synchronous machines. *IEEE Transactions on Energy Conversion*, 27(1):128-138. https://doi.org/10.1109/TEC.2011.2169264

Hsieh MF, Lin CK, Lin IH, 2013. Design and analysis of high temperature superconducting generator for offshore wind turbines. *IEEE Transactions on Magnetics*, 49(5):1881-1884. https://doi.org/10.1109/TMAG.2013.2246146

Kim YB, Hempstead CF, Strnad AR, 1964. Resistive states of hard superconductors. *Reviews of Modern Physics*, 36(1): 43-45. https://doi.org/10.1103/RevModPhys.36.43

Komiya M, Aikawa T, Sasa H, et al., 2019. Design study of 10 MW REBCO fully superconducting synchronous generator for electric aircraft. *IEEE Transactions on Applied Superconductivity*, 29(5):5204306. https://doi.org/10.1109/TASC.2019.2906655

Komiya M, Sugouchi R, Sasa H, et al., 2020. Conceptual design and numerical analysis of 10 MW fully superconducting synchronous generators installed with a novel casing structure. *IEEE Transactions on Applied Superconductivity*, 30(4):5206607. https://doi.org/10.1109/TASC.2020.2989746

Kovalev K, Ivanov N, Tulinova E, et al., 2019. Methodic of calculation of fully HTS salient-pole electrical machine. *Przegląd Elektrotechniczny*, 95(1):213-218. https://doi.org/10.15199/48.2019.01.51

Lee SB, Lee TH, Jung EH, et al., 2014. Development of 250 kV HVDC XLPE cable system in Korea. Proceedings of the International Symposium on Electrical Insulating Materials, p.334-337. https://doi.org/10.1109/ISEIM.2014.6870787

Li Y, Qiu L, Zhi YJ, et al., 2023. An overview of bearing voltages and currents in rail transportation traction motors. *Journal of Zhejiang University-SCIENCE A (Applied Physics & Engineering)*, 24(3):226-242. https://doi.org/10.1631/jzus.A2200180

Liu XH, Wang YY, Luo XM, et al., 2022. Stator single-line-to-ground fault protection for powerformers based on HSGC and CNN. *Frontiers in Energy Research*, 10:998797. https://doi.org/10.3389/fenrg.2022.998797

Liu YZ, Grilli F, Cao JW, et al., 2021. An electromagnetic design of a fully superconducting generator for wind application. *Energies*, 14(22):7811. https://doi.org/10.3390/en14227811

Manolopoulos CD, Iacchetti MF, Smith AC, et al., 2020. Comparison between coreless and yokeless stator designs in fully-superconducting propulsion motors. *IEEE Transactions on Applied Superconductivity*, 30(6):5207407. https://doi.org/10.1109/TASC.2020.2992588

Masson PJ, Luongo CA, 2005. High power density superconducting motor for all-electric aircraft propulsion. *IEEE Transactions on Applied Superconductivity*, 15(2):2226-2229. https://doi.org/10.1109/TASC.2005.849618

Metwally IA, Radwan RM, Abou-Elyazied AM, 2008. Powerformers: a breakthrough of high-voltage power generators.

*IEEE Potentials*, 27(3):37-44.
https://doi.org/10.1109/MPOT.2008.915315

Miller TJE, Hughes A, 1977. Comparative design and performance analysis of air-cored and iron-cored synchronous machines. *Proceedings of the Institution of Electrical Engineers*, 124(2):127-132.
https://doi.org/10.1049/piee.1977.0022

Muttaqi KM, Islam R, Sutanto D, 2019. Future power distribution grids: integration of renewable energy, energy storage, electric vehicles, superconductor, and magnetic bus. *IEEE Transactions on Applied Superconductivity*, 29(2):3800305.
https://doi.org/10.1109/TASC.2019.2895528

Oishi I, Nishijima K, 2002. Summary of development of 70 MW class model superconducting generator––research and development of superconducting for electric power application. *Cryogenics*, 42(3-4):157-167.
https://doi.org/10.1016/S0011-2275(02)00032-2

Perers R, Lundin U, Leijon M, 2007. Development of synchronous generators for Swedish hydropower: a review. *Renewable and Sustainable Energy Reviews*, 11(5):1008-1017.
https://doi.org/10.1016/j.rser.2005.07.007

Seo K, Yoon J, Cha J, et al., 2023. Design optimization of HTS field coils for high power density motors based on continuum sensitivity analysis. *IEEE Transactions on Applied Superconductivity*, 33(5):5202805.
https://doi.org/10.1109/TASC.2023.3268146

Sumption MD, Murphy J, Susner M, et al., 2020. Performance metrics of electrical conductors for aerospace cryogenic motors, generators, and transmission cables. *Cryogenics*, 111:103171.
https://doi.org/10.1016/j.cryogenics.2020.103171

Sun EQ, 2022. Multi-scale nonlinear stress analysis of $Nb_3Sn$ superconducting accelerator magnets. *Superconductor Science and Technology*, 35(4):045019.
https://doi.org/10.1088/1361-6668/ac5a11

Terao Y, Seta A, Ohsaki H, et al., 2019. Lightweight design of fully superconducting motors for electrical aircraft propulsion systems. *IEEE Transactions on Applied Superconductivity*, 29(5):5202305.
https://doi.org/10.1109/TASC.2019.2902323

Tian Q, Lin XN, 2006. A new novel differential protection scheme for a high-voltage, cable-wound generator. IEEE/PES Transmission & Distribution Conference and Exposition: Latin America, p.1-6.
https://doi.org/10.1109/TDCLA.2006.311625

Wang L, Lien SY, Prokhorov AV, 2015. Stability improvement of a large-scale offshore wind farm using a superconducting magnetic energy-storage unit and a superconducting fault-current limiter. IEEE Industry Applications Society Annual Meeting, p.1-7.
https://doi.org/10.1109/IAS.2015.7356927